

The Polyhedral Specular Reflector: A Spectrum-Splitting Multijunction Design to Achieve Ultrahigh (>50%) Solar Module Efficiencies

Carissa N. Eisler , Cristofer A. Flowers, Emily C. Warmann, John V. Lloyd, Pilar Espinet-Gonzalez ,
Sunita Darbe , Michelle S. Dee, Matthew D. Escarra, Emily D. Kosten, Weijun Zhou, and Harry A. Atwater 

Abstract—The most feasible pathway to record 50% efficiency photovoltaic devices is by utilizing many (>4) junctions to minimize thermalization and nonabsorption losses. Here we propose a spectrum-splitting design, the polyhedral specular reflector (PSR), that employs an optical architecture to divide and concentrate incident sunlight, allowing the incorporation of more junctions compared with traditional monolithic architectures. This paper describes the PSR design and indicates the requirements to achieve a 50% efficiency module by coupling robust cell, optical, and electrical simulations. We predict that a module comprised of the seven subcells with an average external radiative efficiency of at least 3%, an optical architecture capable of a splitting efficiency of at least 88% and 300× concentration, small ($\leq 1 \mu\text{m}$) metallic fingers for subcell contact, and a state-of-the-art power conditioning system (>98% efficiency) can achieve a module efficiency of 50%,

a record for both multijunction cells and modules. We also discuss the flexibility of the design and explore how adjusting the size and type of concentrators can still yield record module efficiencies (>40%).

Index Terms—Concentrating, dichroic filter, high efficiency, photovoltaics, spectrum splitting.

I. INTRODUCTION

AS THE effects of climate change escalate, it is more important now than ever to generate high capacity renewable energy resources that can produce a significant portion of our electricity needs. Photovoltaics are well posed to face this challenge because of rapidly declining system costs and modularity [1]. Efficiency is a strong lever for further cost reduction because the power produced affects both module and system costs. While possible, photovoltaic efficiencies exceeding 50% have not yet been realized. The best prospects for achieving such efficiencies are to employ multijunction solar cells, which more effectively convert the broadband solar spectrum than single-junction devices by reducing losses from thermalization of carriers and from not absorbing low energy photons [2]–[5]. However multijunction cells have only achieved a maximum of 46.0% efficiency, limited by the challenge of combining materials and therefore in number of subcells incorporated [6]. Further, once these cells are integrated into a field-ready module with concentrating optics, cell interconnects, and bypass diodes, this efficiency drops to a maximum of 38.9% [6]. Using today’s photovoltaic materials, the best prospects for achieving module efficiencies in excess of 50% involve spectrum-splitting architectures.

The monolithic growth of multiple materials for current multijunction cells necessitates current and lattice matching, resulting in nonideal bandgap choice and fewer subcells total. Structures that allow for spatially and electrically independent subcells have the potential to achieve ultrahigh efficiencies because they avoid these constraints [7]. Additionally, they exhibit better management of radiatively emitted photons and significantly higher average annual energy production over traditional multijunction designs [8], [9]. This is possible through spectrum-splitting architectures that employ an external optical element to divide the incident solar spectrum onto independent subcells [10], [11]. Although these structures have increased complexity because of the spectrum-splitting optics, previous

Manuscript received May 23, 2018; revised August 17, 2018; accepted September 19, 2018. This work was supported in part by the Department of Energy “Light-Material Interactions in Energy Conversion” Energy Frontier Research Center under grant DE-SC0001293, and in part by the Dow Chemical Company through the Full Spectrum Project, and in part by the Advanced Research Projects Agency-Energy, U.S. Department of Energy, under Award Number DE-AR0000333. (Corresponding author: Harry A. Atwater.)

C. N. Eisler was with the Thomas J. Watson Laboratory of Applied Physics, California Institute of Technology, Pasadena, CA 91125 USA. She is now with the Lawrence Berkeley Laboratory, Berkeley, CA 94720 USA (e-mail: carissaeisler@lbl.gov).

C. A. Flowers, E. C. Warmann, J. V. Lloyd, P. Espinet-Gonzalez, and H. A. Atwater are with the Thomas J. Watson Laboratory of Applied Physics, California Institute of Technology, Pasadena, CA 91125 USA (e-mail: cflowers@caltech.edu; warmann@caltech.edu; jvlloyd@caltech.edu; pespinet@caltech.edu; haa@caltech.edu).

S. Darbe was with the Thomas J. Watson Laboratory of Applied Physics, California Institute of Technology, Pasadena, CA 91125 USA. She is now with Spiber Inc., Tsuruoka, Yamagata 997-0052, Japan (e-mail: sdarbe@caltech.edu).

M. S. Dee was with the Thomas J. Watson Laboratory of Applied Physics, California Institute of Technology, Pasadena, CA 91125 USA. She is now with PPG Industries, Inc., Sylmar, CA 91342 USA (e-mail: michelle.s.dee@gmail.com).

M. D. Escarra was with the Thomas J. Watson Laboratory of Applied Physics, California Institute of Technology, Pasadena, CA 91125 USA. He is now with the Department of Physics & Engineering Physics, Tulane University, New Orleans, LA 70118 USA (e-mail: edkcosten@tulane.edu).

E. D. Kosten was with the Thomas J. Watson Laboratory of Applied Physics, California Institute of Technology, Pasadena, CA 91125 USA. She is now with the MIT Lincoln Laboratory, Massachusetts Institute of Technology, Lexington, MA 02420 USA (e-mail: edkosten@mit.edu).

W. Zhou is with the Core R&D-Materials Science and Engineering, Dow Chemical Company, Freeport, TX 77541 USA (e-mail: wzhou2@dow.com).

This paper has supplementary downloadable multimedia material available at <http://ieeexplore.ieee.org> provided by the authors.

Color versions of one or more of the figures in this paper are available online at <http://ieeexplore.ieee.org>.

Digital Object Identifier 10.1109/JPHOTOV.2018.2872109

work has shown that spectrum-splitting submodules with low optical losses, and therefore high efficiencies, are possible [12]–[21]. Most notably, Green *et al.* have demonstrated a >40% efficiency four-junction spectrum-splitting submodule [22]. Although the spectrum-splitting design must incorporate both concentration and spectrum splitting, its efficiency approaches that of the best known monolithic multijunction submodule (43.4%) demonstrated by Steiner *et al.* [23]. Our goal is to design a spectrum-splitting architecture that accommodates many (>4) subcells with an optimized set of bandgaps and achieves an ultrahigh module efficiency.

Here we present such a spectrum-splitting design, the polyhedral specular reflector (PSR), that incorporates seven electrically independent subcells and is capable of >50% module efficiencies. We designed and simulated the spectrum-splitting structure through a comprehensive ray tracing model integrated with modified detailed balance calculations to account for nonideal device physics of the subcells. We validated the modeled spectrum-splitting performance by fabricating and characterizing the designed filter stack. We optimized the concentrator geometries both for ultrahigh efficiencies and for alternative cost-effective designs. Finally, we investigated representative design cases by incorporating additional electrical losses to determine module efficiencies. Ultrahigh module efficiencies (>50%) were found to be possible with this spectrum-splitting design.

II. OPTICAL DESIGN

The spectrum-splitting photovoltaic optical design requires: 1) a highly effective method of dividing the incident spectrum into many bands; and 2) a sufficient degree of concentration to improve subcell performance. The PSR incorporates both of these elements through a series of multilayer dielectric filters to divide the incident spectrum and two stages of concentration. Fig. 1(a) shows schematics of the PSR design. Incident light enters the primary concentrator, either a hollow, mirrored compound parabolic concentrator (CPC) or an acrylic nonimaging lens. The output of the primary concentrator feeds directly into a solid glass prism with seven longpass filters. The filters are oriented at 45° and ordered to sequentially reflect away the highest energy photons. As a result, the incident spectrum is divided into seven bands with the highest energy photons at the top of the prism and the lowest energy photons at the bottom, as shown in Fig. 1(b). Each spectral band is then further concentrated by a solid glass secondary CPC before it is converted by one of the seven subcells. Depending on the relative sizes of the primary and secondary concentrators, these individual units can pack horizontally in-plane as in Fig. 1(c) or vertically in a nonplanar configuration [14], [24]. One could imagine manufacturing this structure by adhering individual components together or by embedding glass filters into a custom injection mold, eliminating the need for many individual components.

A. Bandgap Selection

The bandgaps were chosen based on a detailed balance optimization that included parameters to account for subcell non-ideality [7], [25]. Nonideal current collection and incomplete absorption were incorporated through the collected fraction of

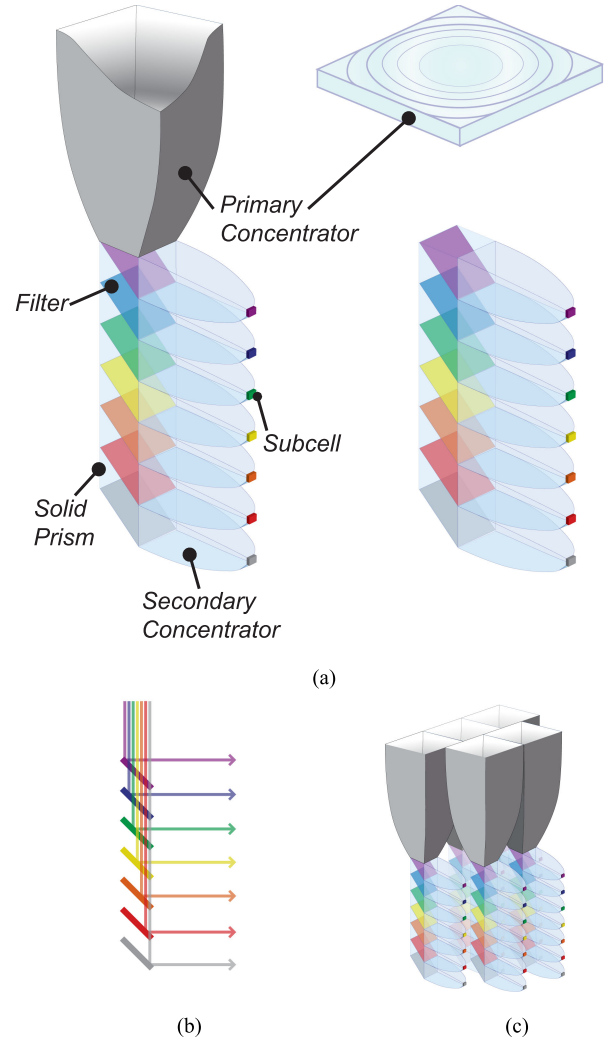


Fig. 1. (a) Schematics of the polyhedral specular reflector (PSR) submodule. Incident light is divided through reflection and transmission by a series of filters embedded in a solid glass prism. Concentration is achieved in two stages. (b) Schematic of light splitting process of the PSR. Longpass filters sequentially reflect away high-to-low energy light for conversion in the appropriate subcell. (c) Schematic of an example horizontal packing of PSR submodules.

ideal short-circuit current density (J_{sc}). Since losses from the antireflection coating will be included in the ray tracing model, this term accounts for all other potential current losses, such as incomplete absorption from a thin ($O(\mu\text{m})$) cell, bulk trap states, parasitic absorption from window layers, interfacial losses, etc. The collected fraction of ideal J_{sc} was calculated to be 92% using external quantum efficiency (EQE) data from a high efficiency GaAs solar cell and assuming 2.8% shadowing losses from the contacts [26]. We note that the shadowing losses from the contacts will depend on the concentration and geometry of the design and we adjust this later when calculating the full module efficiency. Material quality was defined by the external radiative efficiency (ERE) [27] and was estimated from existing photovoltaic devices when available and 1-D device physics simulations supplementally [7], [25], [26], [28]. We chose only III-V alloys for their high potential EREs from high quality material growth and high photon recycling from epitaxial liftoff processes [29]. We determined that a minimum of seven

TABLE I
OPTIMIZED BANDGAPS AND SUGGESTED III-V ALLOYS

E_g (eV)	III-V Alloy	Growth Wafer	ERE (%)
2.13	$\text{Al}_{0.20}\text{Ga}_{0.32}\text{In}_{0.48}\text{P}$	GaAs	0.19
1.78	$\text{Ga}_{0.37}\text{In}_{0.63}\text{P}$	GaAs	8 [28]
1.54	$\text{Al}_{0.1}\text{Ga}_{0.9}\text{As}$	GaAs	3
1.42	GaAs	GaAs	22.5 [26]
1.15	$\text{In}_{0.87}\text{Ga}_{0.13}\text{As}_{0.28}\text{P}_{0.72}$	InP	1.2
0.94	$\text{In}_{0.71}\text{Ga}_{0.29}\text{As}_{0.62}\text{P}_{0.38}$	InP	1.6
0.74	$\text{In}_{0.53}\text{Ga}_{0.47}\text{As}$	InP	11

bandgaps would be required to achieve ultrahigh efficiency with realistic material quality, optical losses, and concentration levels. This large number of subcells represents a significant change from traditional multijunction cells. The final bandgaps with their corresponding EREs and materials are shown in Table I. Modeled EREs assume lattice-matched growth to a commonly available wafer (e.g., GaAs), lifted off subcells, and high quality back reflectors. We note that the highest EREs are from experimental data. The selected bandgaps are slightly modified from the optimum bandgap combination outlined in [25] to achieve lattice matched growth; this had an insignificant effect on the modeled efficiency. Assuming realistic subcell properties and 300 suns concentration, a total efficiency of 57% is expected. Therefore a >50% efficiency module should be possible with high quality optics and a high efficiency power conditioning system.

B. Optical Splitting

The most critical optical component of the PSR is the splitting optic that divides the incident spectrum. Effective division minimizes thermalization and nonabsorption losses that result when photons are misallocated among subcells. We designed seven aperiodic dielectric filters using alternating layers of SiO_2 and TiO_2 because of their high index contrast and high reflectivity. The number and thicknesses of these layers were optimized in OpenFilters to maximize reflection of photons with energies greater than the bandgap of the corresponding subcell and minimize reflection of sub-bandgap photons [30]. Typically these filters had a few hundred layers and a total thickness of 20–35 μm (see Fig. S4, supplemental information). The resulting spectrum-splitting is shown in Fig. 2 (solid lines). The percent of incident photons decreases near the bandgap as a result of *s* and *p* polarization splitting of the filters, which are operating at 45° angle of incidence. The reflectivity cutoff always occurs for an energy higher than the bandgap to ensure that no low energy photons are misallocated to a subcell that cannot convert them. This results in some high energy photons being distributed to lower energy subcells and converted at a lower voltage; however, this loss is far less detrimental than not converting these photons. Thus, a system that uses this series of filters to divide the incident spectrum would produce 94% of the power of a system that has perfect spectrum splitting.

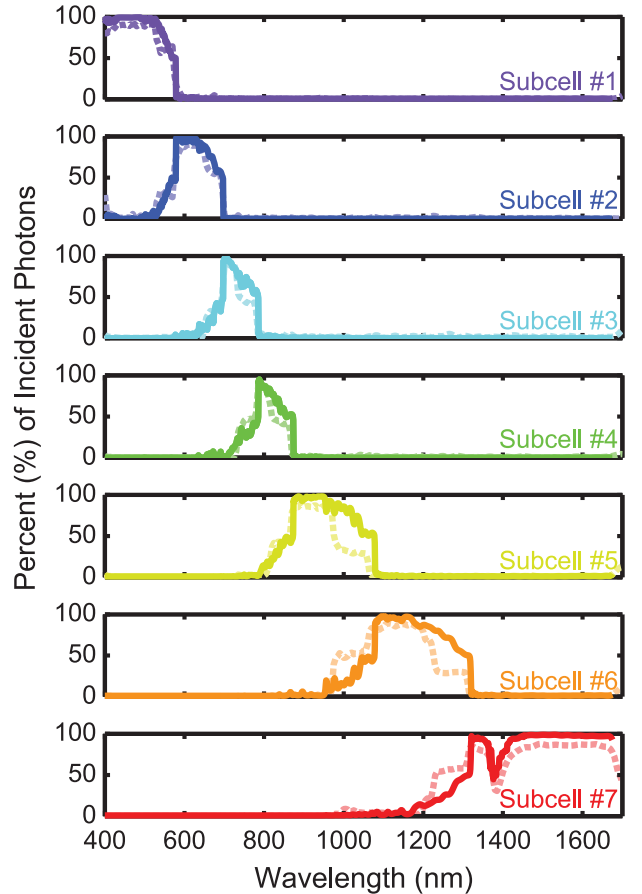


Fig. 2. Percent of incident photons allocated to each subcell from spectrum-splitting optics. The theoretical splitting (solid lines) is from filters consisting of alternating layers of SiO_2 and TiO_2 . An experimental demonstration (dashed lines) from [24] shows spectrum-splitting from a filter stack with similarly designed filters ($\text{SiO}_2/\text{Nb}_2\text{O}_5$ or Ta_2O_5). The expected conversion efficiency of the fabricated filters will be 97% of the designed filters, demonstrating excellent spectrum-splitting experimentally.

The dashed lines in Fig. 2 show the resulting spectrum splitting of a fabricated filter stack using a similar design and materials (Nb_2O_5 and Ta_2O_5 instead of TiO_2) on a Corning HPFS 7980 glass [31]. The difference in high index material used slightly alters the reflectivity profile. The glass substrate creates an absorption band at 1400 nm that should not adversely affect the overall efficiency since it coincides with an absorption band in the terrestrial solar spectrum. Even with these differences, the experimentally demonstrated filters would produce 91% of the power of a perfect system, which is 97% of the efficiency of the original design. This is noteworthy both as validation of the optical modeling and as a peerless demonstration of highly efficient spectrum splitting into many bands.

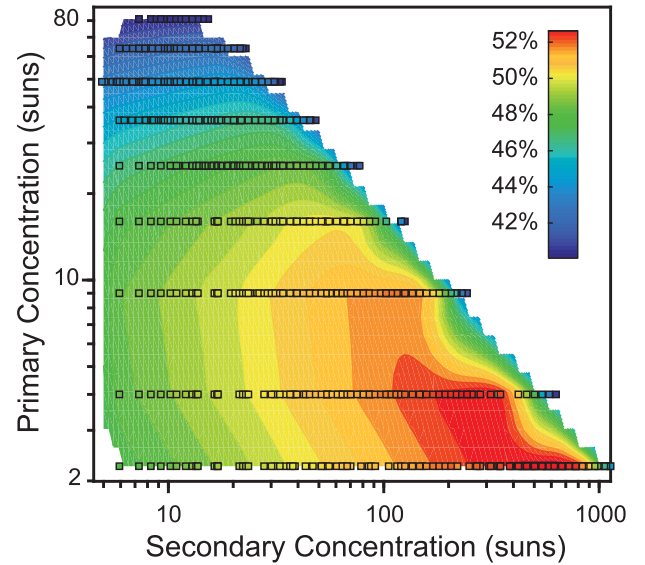
C. Concentration

Further optical design work is necessary since moderate concentration (at least 55 suns) is necessary for >50% module efficiency with these spectrum-splitting optics. For this study, we employed a CPC as the primary concentrator. While Fresnel lenses are more common in deployed multijunction cells, we focused on CPCs here because these concentrators can

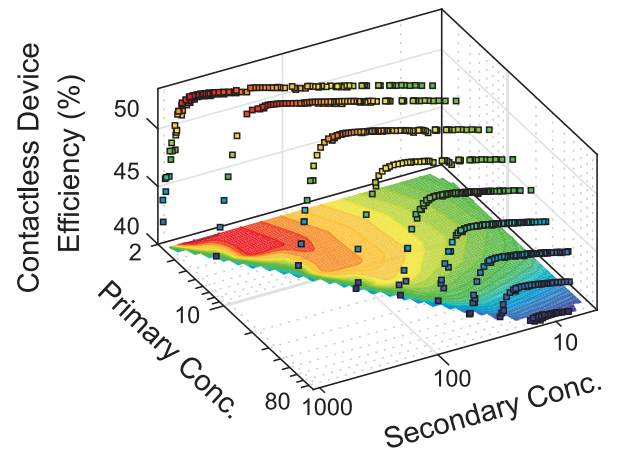
achieve the thermodynamic limit of concentration for a given acceptance angle [32]. We will explore lenses as primary concentrators for select cases later on. Concentration is increased when the acceptance angle decreases or when the output angle increases. This relationship between acceptance and output angle underlies all design tradeoffs in this optical spectrum-splitting architecture. First, our module must accept all photons from the sun and therefore we defined our acceptance angle of the primary concentrator to be 1.8° . This is significantly larger than the disc of the sun to allow for circumsolar radiation and tracking tolerances. Second, the output angle of the primary concentrator will affect the spectrum-splitting efficiency because the spectral splitting performance of the aperiodic dielectric filters is sensitive to incident angle. Increasing the primary concentration, thereby increasing the output angle of the primary concentrator, will decrease the spectrum-splitting efficiency. Finally, the efficiency will decrease if the acceptance angle of the secondary concentrator is smaller than the output angle of the primary concentrator because light will be rejected by the secondary concentrators. The geometries of the primary and secondary concentrators must be optimized together to maximize transfer of incident sunlight to the correct subcells.

We implemented design sweeps to co-optimize the primary and secondary concentrators. We modeled the entire PSR structure in a ray tracing simulation, including a realistic set of optical properties for antireflection coatings (air-glass and glass-subcell interfaces), mirror surfaces, and filter properties, under a broad-band illumination source with 1.5° divergence to account for circumsolar radiation. The size of the optical splitting prism was fixed with a 1×1 cm opening, allowing the primary concentrator input size and secondary concentrator output size to vary. Glass components are assumed to be Corning HPFS 7980 glass, which has a very high internal transmittance, to account for absorption losses. We note that absorption losses are volumetric and will change with the size scale of the module. Further details about the model are discussed in the supplemental. After each simulation, the photon flux to each subcell position was extracted and input to the modified detailed balance calculations to determine the conversion efficiency with optical and cell losses. Because optimizing the contact geometry is computationally intensive, we neglected these losses for now and refer to this efficiency as the contactless device efficiency $\eta_{\text{contactless}}$. We calculate the full module efficiency, which includes electrical losses like power conditioning, for a few select cases later.

Fig. 3 shows different perspectives of the contactless device efficiency of the PSR (color, z -axis) as a function of secondary concentration (x -axis) and primary concentration (y -axis). Each square point represents an individual simulation. The projected contour represents the estimated contactless device efficiency for any concentration combination created by fitting the nearest neighbors of the simulations. Based on previous electrical simulations [33], we expect the efficiency of the electronics to be 95%–98%, therefore contactless device efficiencies exceeding 52% should approach $>50\%$ module efficiencies. Indeed ultrahigh ($>50\%$) efficiency designs are possible with this



(a)



(b)

Fig. 3. (a) 2-D projection. (b) 3-D perspective of the contactless device efficiency as a function of primary and secondary concentration. Each square point represents a ray tracing simulation performed with a CPC for the primary concentrator. The projected contour represents the predicted efficiency for any arbitrary concentration based on these simulations. Contactless device efficiency generally increases with (1) decreasing primary concentration, and (2) increasing secondary concentration.

architecture, with the highest efficiency designs achieved with the combination of low primary concentration and high secondary concentration. This is intuitive because of the nature of the spectrum-splitting optics. A higher primary concentration corresponds to a higher output angle that increases the angular distribution on the aperiodic dielectric filters and reduces the optical splitting efficiency. A higher secondary concentration does not affect the performance of the filters, therefore, in general, increasing the secondary concentration increases the efficiency. However, there is a critical secondary concentration for each primary concentration series that corresponds to the acceptance angle of the secondary concentrator being too small

for the output angle of the associated primary concentrator, as shown by the turnover in efficiency for high values of secondary concentration. Because the secondary concentrators operate via total internal reflection, the losses in the secondary concentrators are primarily because of light leakage and absorption for long concentrators (>100 mm). We also note that designs with higher primary concentration (>36 suns) are capable of record module efficiencies ($>40\%$). These may be attractive as lower cost alternatives that reduce the expensive filter and secondary concentrator volume per module area.

D. Concentrator Truncation

Many of the highest efficiency PSR designs have very long (>300 mm) secondary concentrators that have significant absorption losses and would be difficult to fabricate. Therefore we also investigated trimming the primary and secondary CPCs to maintain high efficiency designs with shorter concentrators [34]. We trimmed these concentrators by removing length near the input side of the CPC where the CPC sidewalls are nearly vertical, resulting in minimally reduced concentration. For the primary concentrator, the input aperture is decreased with increased trimming for the same output angle. For the secondary concentrator, the CPC must be scaled up after trimming to fit onto the solid prism containing the filters, which therefore increases the output aperture and reduces the concentration. We repeated the optimization of the concentrators to achieve high efficiency designs with shorter concentrators whose aspect ratio is at least an order of magnitude smaller than the highest efficiency designs (length < 60 mm).

Fig. 4 shows the contactless device efficiencies of trimmed structures based on a low ($2.25\times$) primary concentration (see Fig. 4(a) and a high ($81\times$) primary concentration (see Fig. 4(b)). In these structures, the output angle of the primary concentrator is fixed at the value corresponding to the untrimmed CPC (2.7° for $2.25\times$, 16.4° for $81\times$), and the different concentration values correspond to different trimmed CPC lengths. We observe the same trend in primary concentration length for both concentration regimes: a longer primary concentrator, and therefore higher primary concentration, results in higher efficiency. This may seem counterintuitive given the trends in Fig. 3, but the primary concentrators in each trimmed study have the same output angle and therefore the optical splitting efficiency is not reduced at higher primary concentrations.

In Fig. 4(a), efficiency generally increases with secondary concentrator length for structures based on low ($2.25\times$) primary concentration length designs. The efficiency decreases beyond 150 mm as absorption losses become significant. We note that $>52\%$ contactless device efficiencies are still possible with concentrators that are significantly shorter (< 60 mm). By contrast, the maximum efficiency for the structures based on the $81\times$ primary concentration design occurs at much shorter concentrator lengths. Additionally, the efficiencies for the trimmed structures are unexpectedly higher than the corresponding untrimmed structures by as much as 3% absolute. This is a result of the geometry of trimmed secondary CPCs, which, when strongly trimmed, resemble a light pipe with straight sidewalls (see

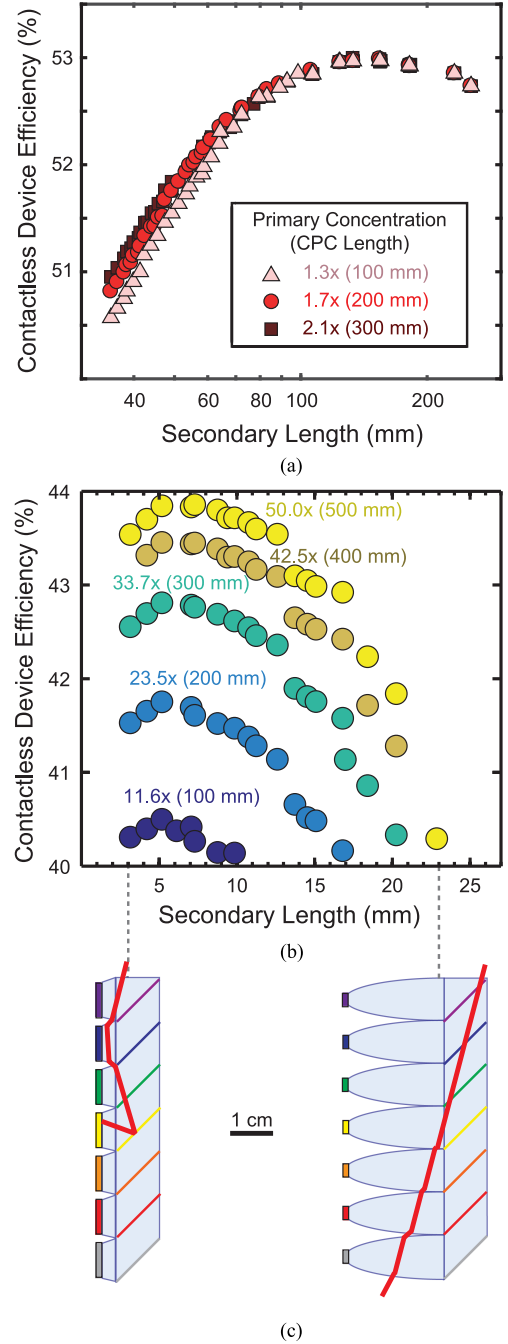


Fig. 4. Contactless device efficiency versus secondary concentrator length for trimmed PSR structures. (a) Efficiencies for a trimmed PSR structure based on the original $2.25\times$ primary concentrator design (2.7° output angle). (b) Efficiencies for a trimmed structure based on the original $81\times$ primary concentrator design (16.4° output angle). (c) Schematics showing the light path for large primary concentration output angles with highly trimmed (left) and untrimmed (right) secondary concentrators. Light is able to refract back into the PSR for highly trimmed concentrators, facilitating the efficiency increase for shorter secondary concentrators.

Fig. 4(c), left). Interestingly, structures with a large primary output angle can direct light to the first secondary concentrator, bypassing the train of filters. This is detrimental for untrimmed structures as the light effectively couples out of the PSR through the mostly horizontal regions of the secondary concentrators

TABLE II
POINT DESIGN CASES FOR MODULE EFFICIENCY PREDICTION

	Case	High Efficiency			High Primary Concentration			
		1	1a	1L	2	2a	2b	2L
Efficiency (%)	Contactless Device Efficiency	50.9	50.7	48.0	42.7	39.4	43.2	42.2
	Optical Efficiency Total	89.0	86.0	83.4	76.4	67.5	73.9	74.4
	<i>Primary Concentrator</i>	95.9	95.8	92.2	95.6	95.5	95.5	91.5
	<i>Spectrum-Splitting Optic</i>	94.1	94.1	92.4	78.1	79.5	84.1	77.1
	<i>Secondary Concentrators</i>	98.5	95.2	97.0	90.4	89.0	92.0	91.5
	<i>Coupling Factor</i>	100	100	100	113	100	100	114
Geometry (suns or mm)	<i>Primary Concentration</i>	1.73	2.25	2.25	50	81	49	90
	<i>(Height)</i>	200	398	265	500	1591	1273	178
	<i>Secondary Concentration</i>	224	664	224	3	12	20	3
	<i>(Height)</i>	64	595	64	7	52	70	7
	<i>Overall Concentration</i>	386	1495	504	155	974	985	180
	<i>Cell Edge Length</i>	0.67	0.39	0.67	5.69	2.88	2.23	5.69

without being converted (see Fig. 4(c), right). For the trimmed structures, light can refract back into the structure because of the higher probability of accessing wider angled surfaces, and light is recovered in the lower bandgap subcells. While none of the trimmed structures based on high primary concentration ($>36\times$) designs achieves $>50\%$ contactless device efficiency, it is important to note that several can achieve record module efficiencies exceeding their untrimmed counterparts.

III. POINT DESIGN CASES

Finally, we modeled the electrical circuits to determine module efficiencies for seven cases of interest. These cases span two regimes from the previous concentration optimization: 1) ultrahigh efficiency ($>50\%$ contactless device efficiency) designs; and 2) high primary concentration (≥ 50 suns) designs that could be lower cost alternatives. We also included two cases that employ a lens (Fresnel or plano-convex) as the primary concentrator for comparison. Additionally, the hollow CPC cases now include a top cover glass, which will introduce a uniform optical loss in the primary concentrators. Table II shows the contactless device efficiency, optical efficiency, and optimized geometries for these designs. Here, we define the optical efficiency ($\eta_{\text{Opt,TOT}}$) as

$$\begin{aligned} \eta_{\text{Opt,TOT}} &= \frac{\eta_{\text{contactless}}(E_g, C, \text{ERE}, f_{J_{sc}})}{\eta_{\text{DB}}(E_g, C, \text{ERE}, f_{J_{sc}})} \\ &= \eta_{\text{Opt,PC}} \eta_{\text{Opt,PSR}} \eta_{\text{Opt,SC}} k. \end{aligned} \quad (1)$$

The optical efficiency represents the accuracy of photon allocation in each PSR geometry as compared with perfect spectrum splitting and concentration [35]. This term shows the total percentage of light absorbed and converted with a penalty for voltage, accounting for the power loss of high energy photons being sent to lower bandgap subcells. Lower energy photons, which see more interfaces and therefore more optical loss, have a smaller contribution to the optical efficiency because they contribute less power than the higher energy photons. We can expand the optical efficiency into

individual components, representing the primary concentrator ($\eta_{\text{Opt,PC}}$), the spectrum-splitting filter train ($\eta_{\text{Opt,PSR}}$), the secondary concentrators ($\eta_{\text{Opt,SC}}$), and a coupling factor (k) to account for any skew rays that are collected for certain geometries with regards to Fig. 4. These individual component optical efficiencies are calculated by including additional receivers in the ray tracing simulations to determine the light collected at each stage. This equation encapsulates the challenge of spectrum-splitting designs: all optical components must be efficient at transferring photons to the correct location. Otherwise, the total conversion efficiency reduces significantly.

Cases 1 and 1a are representative cases of the ultrahigh efficiency regime, where Case 1 is a design for prototyping (trimmed) and Case 1a is the maximum efficiency design for comparison (untrimmed). Although Case 1 has a much smaller concentration than Case 1a ($336\times$ compared with $1495\times$), Case 1 (50.9%) has a contactless device efficiency greater than Case 1a (50.7%) owing to its very high optical efficiency. The optical efficiencies of the primary concentrator and the spectrum-splitting are nearly identical for Cases 1 and 1a because the primary concentrator is nearly the same, yielding a high efficiency spectrum-splitting profile (94%). However the optical efficiency of the secondary concentration stage is higher for Case 1 because Case 1 has trimmed concentrators and significantly less absorption loss.

Cases 2, 2a, and 2b correspond to the high primary concentration regime. We note that these designs can potentially achieve record module efficiencies. Case 2 is an optimized trimmed design based on the $81\times$ primary concentrator structure. Case 2a is the highest efficiency design for the untrimmed $81\times$ primary concentration series, and Case 2b is the optimum design from the untrimmed $49\times$ primary concentration series. Cases 2, 2a, and 2b have similar optical efficiencies through the primary concentration stage (95.5%) as the photon transfer is mostly determined by the reflectivity of the silver coating. The spectrum-splitting optical efficiency is almost identical between Cases 2 and 2a (78.1 and 79.5%, respectively) because these two designs have the same primary concentration output angle. Con-

sequently, Case 2b has a higher spectrum-splitting optical efficiency (84.1%) because it has a lower primary concentration output angle. While the optical efficiency of the secondary concentrators is very similar for all three cases, the coupling factor is greater than 1 for Case 2 because of the refraction effect discussed previously. None of the untrimmed CPC case study designs exhibits this effect and hence have $k = 100\%$. As a result, the optical efficiency for Case 2 (76.4%) more closely matches Case 2b (73.9%) over Case 2a (67.5%), yielding a higher efficiency overall despite a significantly lower concentration.

We additionally investigated a lens as a substitute primary concentrating optic as lenses are far more commonly deployed in concentrating modules. We designed poly(methyl methacrylate) (PMMA) lenses and substituted them in the ray tracing simulation file of the existing Case 1 and Case 2 designs to determine the new contactless device efficiency and optical efficiencies. Case 1L employs a plano-convex lens while Case 2L employs a Fresnel lens. In both cases, the acceptance angle is reduced to 1° (versus 1.8° for CPC) to more closely replicate current concentrating photovoltaic (CPV) technologies [36]. For a consistent comparison, the output angle of the lens is the same as the original CPC. As a result, only the primary concentration and total optical efficiencies change significantly between the original and lens designs. While both concentrators now have Fresnel losses, the optical efficiency of a lens is lower (92%) owing to the PMMA absorption losses. This reduces the contactless device efficiencies for Cases 1L and 2L by 1–2 absolute percent. Despite these losses, Case 2L is still more efficient than Case 2a, and Cases 1L and 2L are capable of record module efficiencies.

A. Electrical Design

We then calculated the electrical losses for each case study using 1) a three-dimensional (3-D) distributed circuit model for top contact geometry optimization and resistive losses; 2) analytic determination of resistive interconnection losses; and 3) California Energy Commission (CEC) weighted efficiency specifications for commercially available power conditioning and circuit combination losses. The distributed circuit model was implemented in Synopsys' simulation program with integrated circuit emphasis (HSPICE) and is described in detail in the supplemental [37]. The contact geometry was independently optimized for every subcell in each case study for contact features with square cross-sections ranging in width from 1–5 μm . Contacts employed in the concentrating photovoltaic industry commonly employ a minimum feature size in the 3–10 μm range, although features as small as 1 μm and below are achievable with photolithography [37]–[41]. Contact designs were constrained to inverted square geometries [42]. The optimization was performed by varying the number of contact fingers at the interior of the cell in order to balance resistive losses from lateral conduction with optical shading from the grid features. In cases where the shadowed fraction differed from that assumed previously (2.8%), the detailed balance calculation and contact optimization were iterated until the calculated shadowed fractions converged. Resistive losses external to

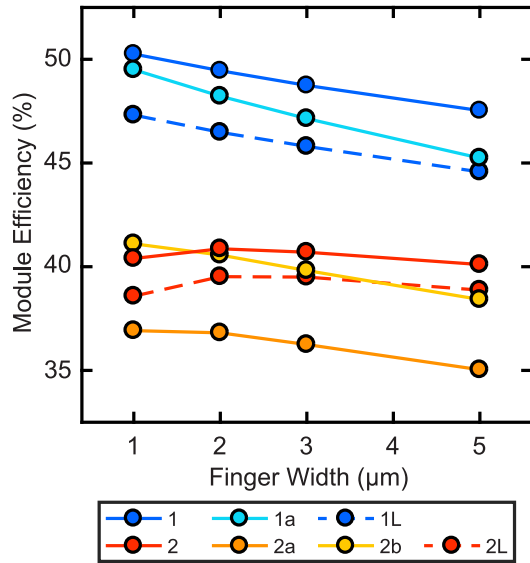
the cells are dependent on wire gauge, module spacing, and sub-cell current output and can, in general, be designed to be small relative to the contact and power conversion losses. This external resistive loss was calculated to be 0.3% for the Case 1 point design and assumed constant across all cases because of design flexibility and low relative contribution to net loss. Finally, state-of-the-art dc power optimizers achieving up to 98.8% weighted efficiency were used to facilitate power combination between subcircuits consisting of series-parallel connected subcells at each bandgap [33], [43].¹ Performance was assumed constant across all design cases.

Fig. 5 shows the optimized module efficiency as a function of contact finger feature size for each of the case studies (see Fig. 5(a)), along with the fractional contribution of each of the electrical and shadowing losses for contact optimizations with 1 and 3 μm features (see Fig. 5(b)). Case 1 is capable of producing an ultrahigh efficiency module with small (1 μm) contact features. Additionally, Cases 2, 2b, and 2L illustrate a range of higher primary concentration designs with record module efficiencies.

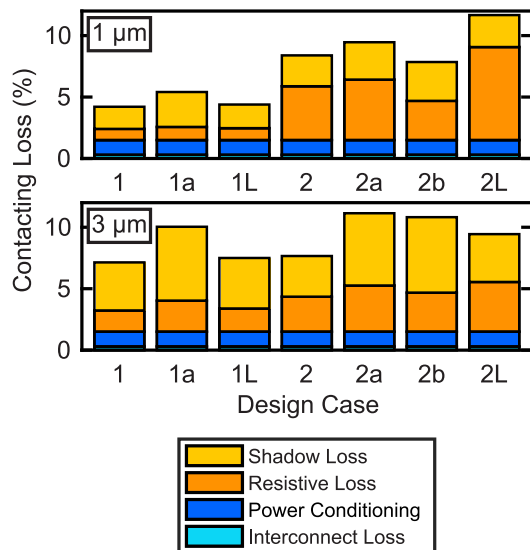
The efficiency versus feature size curves in Fig. 5(a) can generally be divided into two regimes of negative and positive slope. To understand each of these regimes, first consider that the optimum contact geometry occurs where the rate of increase in obscured area or “shadow” losses from adding additional contact fingers equals the rate of decrease in contact resistive losses. Further, the contact resistive losses are comprised of resistance to lateral conduction in the emitter sheet, contact resistance at the semiconductor-metal interface, resistivity of the metal fingers, and resistivity of the busbar. The ratio of electrical to shadow loss varies by cell size and concentration regime. Lower concentration designs are less sensitive to contact feature sizes according to the quadratic relationship between current and resistive power loss in the contacts ($P = I^2R$). This relationship dictates a steeper slope to the efficiency versus contact feature size curves for designs with higher overall concentration. For example, this quadratic loss relationship enables the trimmed, lower concentration Case 1 to have a less negative slope and therefore smaller electrical losses at larger contact finger sizes. Most of the cases considered fall within this regime of increasing efficiency with decreasing finger width. In this regime, the resistive losses are dominated by the lateral sheet resistance of the device emitter layer. Thus, decreasing the finger width increases the optimal number of fingers to decrease finger-to-finger spacing, parallelizes current collection and reduces sheet resistance loss while simultaneously reducing the total shadowed area. The sheet resistance dominated loss regime is most apparent for cases 1, 1a, 1L, and 2b in Fig. 5(b). These cases show mutual reduction of both resistive and shadow loss for 1 μm optimized contact features relative to 3 μm optimized contact features.

In contrast, the regions of positive slope correspond to regimes where the finger and busbar resistive losses are sufficiently large to dominate the aggregate shadow and resistive loss.

¹The cited P-600 series dc power optimizer, which was used in the design, is no longer in production. A similar design can be performed with the P-300 series power converters.



(a)



(b)

Fig. 5. Module efficiency accounting for optical and electrical losses for the seven design cases described in Table II. (a) Module efficiencies for the design cases as a function of contact feature size. Each datum accounts for uniquely simulated contact geometries and resistive and power conditioning losses external to the subcells. (b) Breakout of the absolute power loss in the 1 and 3 μm optimizations of each design case. Losses result from the top contact grid shadowing, aggregate resistive contact grid loss, power conditioning for subcell power combination, and subcell interconnection wiring resistive loss.

Maintaining constant aspect ratio has the side effect of constraining the entire contact metallization thickness, thereby increasing the finger and busbar resistances. In cases of high current, most notably in those with larger cell sizes that have higher resistance because of conduction length, decreasing the feature size results in reduced shadow and emitter sheet resistive loss, but a net increase to resistive and cumulative loss, and consequently lower efficiency. Cases 2 and 2L exhibit resistive loss dominated contact metallization; both the ratio of resistive to shadow loss and the net loss increase as the feature size is decreased. Lastly,

Case 2a represents a transitional case between the aforementioned regimes. The ratio of resistive to shadow loss increases significantly with decreasing feature size, but the net loss is reduced. This transitional region at the smallest feature size considered corresponds to the leveling out of slope of the Case 2(a) curve in Fig. 5(a).

These mechanisms serve to identify a few areas of future interest broadly applicable to concentrating photovoltaics. First, there is substantial potential for increased efficiency by driving toward small cells and fine contact features. Second, an optimum contact feature size exists given the specific aspect ratio constraints of a given contact patterning process and the geometrical parameters of the cell and concentration employed. Finally, this optimum can be improved by developing processes for higher aspect ratio contacts, thereby reducing resistive loss in the contact metallization and expanding the potential for improved efficiency.

IV. CONCLUSION

This paper has developed a spectrum-splitting structure, the PSR, and modeled its potential module efficiency from a system level perspective. We have accounted for the realistic losses in a photovoltaic module by integrating detailed balance calculations, wave optics simulations, ray tracing simulations, and 3-D distributed circuit modeling. We have also developed a parametric equation that can be used to predict the efficiency of this spectrum-splitting design by knowing the efficiency of photon allocation (optical efficiency) for each optical component, and map out a wide design space. From these models, we have shown that record efficiencies and even ultrahigh ($>50\%$) efficiencies are possible using cell, optical, and electrical technologies already available to us. We predict a seven-junction module can achieve 50% efficiency as long as the ensemble averaged ERE of the subcells is at least 3%. Such EREs are possible for very low defect, off-substrate solar cells explored in the III-V cell community [26], [28]. Additionally, the optical architecture that splits and concentrates light must have an optical efficiency near 90%. We have shown here that high optical efficiency is both theoretically and experimentally possible using traditional multilayer dielectric stack filters, but is strongly dependent on the concentration prior to splitting. Therefore, a low primary concentration ($<10\times$) and high secondary concentration ($>100\times$) is recommended for high optical efficiencies. Finally, an ultrahigh efficiency module necessitates a high efficiency electrical system to effectively extract and combine the power generated from each subcell with minimal shadowing and resistive losses. Small, optimized contact feature sizes ($\leq 1 \mu\text{m}$) and state-of-the-art power converters ($>98\%$ efficiency) constitute an electrical architecture sufficient for 50% efficiency solar modules. Through this study, we hope to inspire new and disruptive multijunction cell and module architectures that push the limits of photovoltaic module efficiency.

ACKNOWLEDGMENT

The authors would like to thank Dr. R. Pala for his guidance in setting up the optical characterization. Optical design was

supported by a partnership between the DOE “Light-Material Interactions in Energy Conversion” Energy Frontier Research Center under Grant DE-SC0001293 and the Dow Chemical Company through the Full Spectrum Project. Bandgap selection and electrical design was supported by the Advanced Research Projects Agency-Energy, U.S. Department of Energy, under Award Number DE-AR0000333. C.N.E. was supported by the Department of Defense through the National Defense Science & Engineering Graduate Fellowship Program. C.A.F. was supported by the National Science Foundation Graduate Research Fellowship under Grant No. DGE1144469.

REFERENCES

- [1] M. Woodhouse *et al.*, “On the path to sunshot: The role of advancements in solar photovoltaic efficiency, reliability, and costs,” National renewable energy laboratory (NREL), Golden, CO, USA, Tech. Rep. NREL/TP-6A20-65872, 2016.
- [2] C. H. Henry, “Limiting efficiencies of ideal single and multiple energy gap terrestrial solar cells,” *J. Appl. Phys.*, vol. 51, no. 8, pp. 4494–4500, 1980.
- [3] A. Martí and G. L. Araújo, “Limiting efficiencies for photovoltaic energy conversion in multigap systems,” *Sol. Energy Mater. Sol. Cells*, vol. 43, no. 2, pp. 203–222, 1996.
- [4] G. Araújo and A. Martí, “On the detailed balance limit of ideal multiple bandgap solar cells,” in *Proc. Conf. Rec. 22nd IEEE Photovolt. Specialists Conf.*, 1991, pp. 290–294.
- [5] A. Polman and H. A. Atwater, “Photonic design principles for ultrahigh-efficiency photovoltaics,” *Nature Mater.*, vol. 11, no. 3, pp. 174–177, 2012.
- [6] M. A. Green *et al.*, “Solar cell efficiency tables (version 51),” *Prog. Photovolt.: Res. Appl.*, vol. 26, no. 1, pp. 3–12, 2017.
- [7] E. C. Warmann *et al.*, “Design of photovoltaics for modules with 50% efficiency,” *Energy Sci. Eng.*, vol. 5, pp. 69–80, 2017.
- [8] C. N. Eisler, Z. Abrams, M. T. Sheldon, X. Zhang, and H. A. Atwater, “Multijunction solar cell efficiencies: Effect of spectral window, optical environment and radiative coupling,” *Energy Environmental Sci.*, vol. 7, no. 11, pp. 3600–3605, 2014.
- [9] E. C. Warmann and H. A. Atwater, “Energy production advantage of independent subcell connection for multijunction photovoltaics,” *Energy Sci. Eng.*, vol. 4, no. 4, pp. 235–244, 2016.
- [10] A. Imenes and D. Mills, “Spectral beam splitting technology for increased conversion efficiency in solar concentrating systems: A review,” *Sol. Energy Mater. Sol. Cells*, vol. 84, no. 1, pp. 19–69, 2004.
- [11] A. Mojiri, R. Taylor, E. Thomsen, and G. Rosengarten, “Spectral beam splitting for efficient conversion of solar energy—a review,” *Renewable Sustain. Energy Rev.*, vol. 28, pp. 654–663, 2013.
- [12] B. Mitchell *et al.*, “Four-junction spectral beam-splitting photovoltaic receiver with high optical efficiency,” *Prog. Photovolt.: Res. Appl.*, vol. 19, no. 1, pp. 61–72, 2011.
- [13] A. Barnett *et al.*, “50% efficient solar cell architectures and designs,” in *Proc. IEEE 4th World Conf. Photovolt. Energy Conf.*, 2006, vol. 2, pp. 2560–2564.
- [14] C. N. Eisler *et al.*, “Design improvements for the polyhedral specular reflector spectrum-splitting module for ultra-high efficiency (>50%),” in *Proc. IEEE 40th Photovolt. Specialist Conf.*, 2014, pp. 2224–2229.
- [15] C. N. Eisler, E. D. Kosten, E. C. Warmann, and H. A. Atwater, “Spectrum splitting photovoltaics: Polyhedral specular reflector design for ultra-high efficiency modules,” in *Proc. IEEE 39th Photovolt. Specialists Conf.*, 2013, pp. 1848–1851.
- [16] E. D. Kosten, J. Lloyd, E. Warmann, and H. A. Atwater, “Spectrum splitting photovoltaics: Light trapping filtered concentrator for ultrahigh photovoltaic efficiency,” in *Proc. IEEE 39th Photovolt. Specialists Conf.*, 2013, pp. 3053–3057.
- [17] M. D. Escarra, S. Darbe, E. C. Warmann, and H. A. Atwater, “Spectrum-splitting photovoltaics: Holographic spectrum splitting in eight-junction, ultra-high efficiency module,” in *Proc. IEEE 39th Photovolt. Specialists Conf.*, 2013, pp. 1852–1855.
- [18] X. Wang *et al.*, “Lateral spectrum splitting concentrator photovoltaics: Direct measurement of component and submodule efficiency,” *Prog. Photovolt.: Res. Appl.*, vol. 20, no. 2, pp. 149–165, 2012.
- [19] “Light trapping, a new approach to spectrum splitting,” *Sol. Energy Mater. Sol. Cells*, vol. 92, no. 12, pp. 1570–1578, 2008.
- [20] M. A. Green and A. Ho-Baillie, “Forty three per cent composite split-spectrum concentrator solar cell efficiency,” *Prog. Photovolt.: Res. Appl.*, vol. 18, no. 1, pp. 42–47, 2010.
- [21] J. D. McCambridge *et al.*, “Compact spectrum splitting photovoltaic module with high efficiency,” *Prog. Photovolt.: Res. Appl.*, vol. 19, no. 3, pp. 352–360, 2011.
- [22] M. A. Green *et al.*, “40% efficient sunlight to electricity conversion,” *Prog. Photovolt.: Res. Appl.*, vol. 23, no. 6, pp. 685–691, 2015.
- [23] M. Steine *et al.*, “43% direct sunlight conversion efficiency using 4j cells with achromatic full glass lens,” *AIP Conf. Proc.*, vol. 1766, no. 1, 2016, Art. no. 080006.
- [24] R. J. Linderman, Z. S. Judkins, M. Shoecraft, and M. J. Dawson, “Thermal performance of the SunPower Alpha-2 PV concentrator,” *IEEE J. Photovolt.*, vol. 2, no. 2, pp. 196–201, Apr. 2012.
- [25] E. C. Warmann *et al.*, “Spectrum splitting photovoltaics: Materials and device parameters to achieve ultrahigh system efficiency,” in *Proc. IEEE 39th Photovolt. Specialists Conf.*, 2013, pp. 1922–1925.
- [26] B. M. Kayes *et al.*, “27.6% conversion efficiency, a new record for single-junction solar cells under 1 sun illumination,” in *Proc. 37th IEEE Photovolt. Specialists Conf.*, 2011, pp. 000 004–000 008.
- [27] M. A. Green, “Radiative efficiency of state-of-the-art photovoltaic cells,” *Prog. Photovolt.: Res. Appl.*, vol. 20, no. 4, pp. 472–476, 2012.
- [28] J. F. Geisz, M. A. Steiner, I. Garcia, S. R. Kurtz, and D. J. Friedman, “Enhanced external radiative efficiency for 20.8% efficient single-junction GaInP solar cells,” *Appl. Phys. Lett.*, vol. 103, no. 4, pp. 041118–1–041118-5, 2013.
- [29] O. D. Miller, E. Yablonovitch, and S. R. Kurtz, “Strong internal and external luminescence as solar cells approach the Shockley–Queisser limit,” *IEEE J. Photovolt.*, vol. 2, no. 3, pp. 303–311, Jul. 2012.
- [30] S. Larouche and L. Martinu, “Openfilters: Open-source software for the design, optimization, and synthesis of optical filters,” *Appl. Opt.*, vol. 47, no. 13, pp. C219–C230, 2008.
- [31] C. N. Eisler *et al.*, “Designing and prototyping the polyhedral specular reflector, a spectrum-splitting module with projected >50% efficiency,” in *Proc. IEEE 42nd Photovolt. Specialist Conf.*, 2015, pp. 1–5.
- [32] W. T. Welford and R. Winston, *High Collection Nonimaging Optics*. San Diego, California: Academic Press, Inc., 2012.
- [33] C. A. Flowers, C. N. Eisler, and H. A. Atwater, “Electrically independent subcircuits for a seven-junction spectrum splitting photovoltaic module,” in *Proc. IEEE 40th Photovolt. Specialist Conf.*, 2014, pp. 1339–1343.
- [34] A. Rabl, “Optical and thermal properties of compound parabolic concentrators,” *Sol. Energy*, vol. 18, no. 6, pp. 497–511, 1976.
- [35] J. M. Russo *et al.*, “Spectrum splitting metrics and effect of filter characteristics on photovoltaic system performance,” *Opt. Express*, vol. 22, no. S2, pp. A528–A541, Mar. 2014.
- [36] B. Furman *et al.*, “A high concentration photovoltaic module utilizing micro-transfer printing and surface mount technology,” in *Proc. 35th IEEE Photovolt. Specialists Conf.*, 2010, pp. 000 475–000 480.
- [37] M. Steiner, S. P. Philipps, M. Hermle, A. W. Bett, and F. Dimroth, “Validated front contact grid simulation for gaas solar cells under concentrated sunlight,” *Prog. Photovolt.: Res. Appl.*, vol. 19, no. 1, pp. 73–83, 2011.
- [38] A. Antonini *et al.*, “Contact grid optimization methodology for front contact concentration solar cells,” *Sol. Energy Mater. Sol. Cells*, vol. 80, no. 2, pp. 155–166, 2003.
- [39] J. S. Ward *et al.*, “High aspect ratio electrodeposited Ni/Au contacts for GaAs-based III–V concentrator solar cells,” *Prog. Photovolt.: Res. Appl.*, vol. 23, no. 5, pp. 646–653, 2015.
- [40] I. Garcia, I. Rey-Stolle, B. Galiana, and C. Algora, “A 32.6% efficient lattice-matched dual-junction solar cell working at 1000 suns,” *Appl. Phys. Lett.*, vol. 94, no. 5, 2009, Art. no. 053509.
- [41] A. del Campo and C. Greiner, “SU-8: A photoresist for high-aspect-ratio and 3D submicron lithography,” *J. Micromechanics Microengineering*, vol. 17, no. 6, pp. R81–R95, 2007.
- [42] A. Moore, “Optimized grid design for a sun-concentrator solar cell,” *RCA Rev.*, vol. 40, no. 2, pp. 140–152, 1979.
- [43] SolarEdge, Power optimizer specifications—p600/p700. [Online]. Available: <https://www.solaredge.com/sites/default/files/se-p-series-commercial-add-on-power-optimizer-datasheet.pdf>